Sentinel-1-Aided Mutual Calibration of TanDEM-X DEMs for the Estimation of Height and Volume Changes

Carolina González, *Member, IEEE*, Luca Dell'Amore, José-Luis Bueso-Bello, Pietro Milillo, *Senior Member, IEEE*, Gabriele Schwaizer, Thomas Nagler, *Member, IEEE*, and Paola Rizzoli, *Member, IEEE*

***Abstract*—Digital elevation models (DEM) derived from TanDEM-X single-pass interferometric SAR data are widely used for a large vary of applications. One of the main application fields regards the monitoring of topographic changes, which can be properly estimated by differentiating two DEM scenes acquired at different times. In this scenario, a critical aspect is represented by the precise mutual calibration of the two DEMs, which are normally affected by residual offsets and tilts caused by uncertainties in the baseline determination. This calibration is in general performed by utilizing reference tie-points, whose location and height is known *a priori*, or estimated through other reference sensors, such as GPS or LiDAR data. The manual procedure is time-consuming and can be jeopardized by the absence of available external reference points. In this article, we present a novel technique for performing an automatic selection of reliable natural tie-points from Sentinel-1 repeat-pass time-series, by exploiting persistent scatterers candidates, and we discuss their applicability to TanDEM-X data. We propose a novel method for retrieving a set of reliable natural calibration targets and for performing an effective mutual calibration of TanDEM-X time-tagged DEMs. The approach is validated by considering the estimation of lava field volumes in the test-case scenario of the volcanic eruptions in the Reykjanes Peninsula, Iceland, occurred between 2021 and 2023. Thanks to the continuous global coverage of Sentinel-1, this approach can be applied when no *a priori* knowledge on reference tie-points is available, allowing for the precise estimation of height and volume changes.**

***Index Terms*—Digital elevation model (DEM) calibration, Iceland, lava volume, persistent scatterers (PS), Sentinel-1, synthetic aperture radar interferometry (SAR), TanDEM-X (TDX).**

Received 12 June 2024; revised 23 September 2024 and 8 November 2024; accepted 11 December 2024. Date of publication 23 December 2024; date of current version 17 January 2025. This work was supported in part by the ESA EXPRO+ AlpSnow Project under Grant 4000132770/20/I-NB, in part by the University of Houston under a contract with the NASA Decadal Survey Incubation Program under Grant 80NSSC22K1096, and in part by Science and Technology under Grant NNH21ZDA001N-DSI. *(Corresponding author: Carolina González.)*

Carolina González, Luca Dell'Amore, José-Luis Bueso-Bello, and Paola Rizzoli are with Microwaves and Radar Institute, German Aerospace Center (DLR), 82234 Wessling, Germany (e-mail: carolina.gonzalez@dlr.de; luca.dellamore@dlr.de; jose-luis.bueso-bello@dlr.de; paola.rizzoli@dlr.de).

Pietro Milillo is with Microwaves and Radar Institute, German Aerospace Center (DLR), D-51147 Koeln, Germany, and also with the Department of Civil and Environmental Engineering and the Department of Earth and Atmospheric Science, University of Houston, Houston, TX 77023 USA (e-mail: pmilillo@central.uh.edu).

Gabriele Schwaizer and Thomas Nagler are with ENVEO-Environmental Earth Observation IT GmbH, 6020 Innsbruck, Austria (e-mail: gabriele.schwaizer@enveo.at; thomas.nagler@enveo.at).

Digital Object Identifier 10.1109/JSTARS.2024.3521123

I. Introduction

Digital elevation models (DEMs) derived from spaceborne remote sensing sensors are the current state of the art for mapping the Earth's topography at high resolution. In particular, synthetic aperture radar across-track interferometry (InSAR) is one of the most used techniques for the retrieval of ground topography [1]. It exploits the phase difference between two radar images characterized by a certain spatial diversity, which is generated by the presence of a mutual displacement, called baseline, between the sensors position in the across-track direction at the time of the acquisition.

In particular, single-pass InSAR makes use of two simultaneous acquisitions which are unaffected by temporal changes on ground, since there is no time span in between the surveys. This represents the ideal configuration for topography retrieval, since it avoids temporal signal decorrelation: a source of noise which significantly impacts the quality of repeat-pass interferograms and jeopardize their use [2]. Currently, the TanDEM-X (TDX) mission, which comprises two twin SAR satellites, namely TerraSAR-X (TSX) and TDX, flying in a close bistatic configuration [3], [4], is the only spaceborne bistatic mission at X-band able to deliver single-pass data at variable baselines. Started in 2010, the main goal of the mission was the generation of a global DEM at 12 m resolution, which was successfully delivered in 2016 [5], [6]. The global TDX DEM is the result of the mosaicking of multiple overlapping acquisitions and was calibrated using reference IceSAT light detection and ranging (LiDAR) measurements [7].

Beside the acquisitions used for the generation of the global DEM product, TDX has also been acquiring a large number of subsequent bistatic data takes, which can be used to quantify topographic changes through DEM differentiation. For example, a new global coverage has been performed between 2017 and 2019 and the data have been used for the generation of a new global change DEM product [8].

Moreover, for scientific applications based on DEM differentiation, a precise horizontal and vertical mutual calibration of the considered DEMs is a crucial step. In some cases, residual

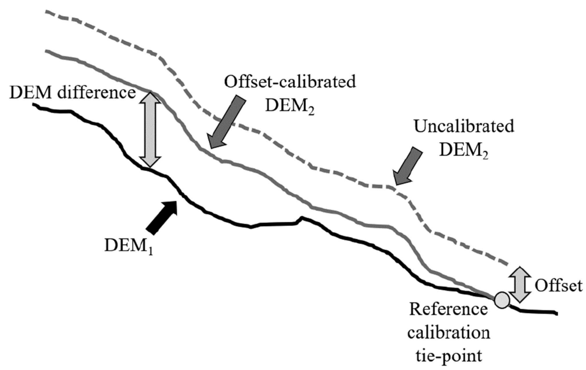

Fig. 1. Schematic representation of DEM mutual calibration using an external reference calibration TP (e.g., GPS or LiDAR measurement) to compensate for residual offsets.

horizontal shifts, vertical offsets, and tilts might be present in the data, which are primarily caused by uncertainties on the knowledge of the satellites orbit position and their variations along the acquisition [3], [9]. One should be aware that TDX bistatic data takes are not systematically affected by these issues, nevertheless it is not possible to predict them *a priori*. This matter is normally tackled prior to performing DEM differentiation, on the one hand, by performing a precise spatial coregistration of the geocoded DEMs, and, on the other hand, either without performing any mutual vertical adjustment or by identifying reliable calibration tie-points (TPs), such as ground positioning system (GPS) or LiDAR measurements, which can be used to vertically adjust the DEMs through an offset compensation, as depicted in Fig. 1. The acquisition of these kinds of reference measurements, which need to be timely consistent with the TDX acquisitions, is often expensive and problematic, especially when remote or scarcely accessible regions are considered. Furthermore, the correction for slowly varying tilts and trends is not possible. Examples in the literature concern different application fields, ranging from the estimation of volcanic lava fields and domes [10], [11], glaciers mass balance and surface change monitoring [12], [13], penetration bias estimation [14], [15], up to forest height and above-ground biomass changes quantification [16], [17], and landslides monitoring [18]. Theoretically, residual offsets and tilts between two overlapping DEMs could also be computed by simply differentiating the entire area and then extrapolating a certain residual calibration surface. This approach is operationally used within the TDX mission for the calibration of the interferometric baselines and it is performed over extremely stable monitoring areas characterized by the presence of bare soil only [9]. In practice, this approach is highly unreliable for scientific applications, as it could be biased by several factors. For example, the presence of volumetric targets, such as vegetation or snow coverage, causes a certain amount of penetration of the radar waves, which depends on both the sensor parameters (such as frequency and incidence angle) and the characteristics of the target itself (e.g., different penetrations are expected into canopies depending on vegetation density, presence of gaps and leaf-on/leaf-off conditions). This could result in a different location of the topographic height corresponding to the InSAR mean phase center within the two considered DEMs, leading to nonnegligible calibration errors. Moreover, further inaccuracies could be caused, e.g., by temporal changes occurred in between the acquisition dates of the two DEMs.

In this article, we propose a novel approach for mutually calibrating single-pass InSAR DEMs using natural TPs, which are derived from time-series of repeat-pass InSAR data. Such TPs are used for the estimation of a calibration surface, which allows for the removal of both, constant vertical offsets and residual tilts. This approach is fully automatic and does not require for the availability of external reference measurements, such as GPS or LiDAR data. The capabilities of the method are demonstrated using TDX bisatic InSAR data for the generation of DEMs, while Sentinel-1 time-series are considered as exemplary repeat-pass InSAR data.

In particular, the Sentinel-1 mission has been specifically designed for repeat-pass interferometric applications, such as differential InSAR and persistent scatterers interferometry (PSI) [19]. It shows an optimal configuration, with two satellites flying on the same nominal orbit, for the retrieval of repeat-pass InSAR acquisitions with nominally negligible across-track baselines. Moreover, the nominal mission acquisition plan foresees a revisit time of only six days over Europe and selected test areas and of 12 days for the rest of the world. At the current date, only one satellite (Sentinel-1 A) is operational, reducing the revisit time to 12 days worldwide. This allows for the continuous acquisition of InSAR time-series at global scale and, consequently, for the application of the proposed algorithm worldwide. Differently, the TDX mission, on the one hand, has the peculiarity of acquiring bistatic InSAR data, which allows for the generation of high-quality DEMs, on the other hand, is not designed for the regular acquisition of long InSAR time-series at large scale, given the limited onboard resources. This aspect does not allow for the sole use of TDX for the application of the proposed methodology, necessitating therefore combination of both missions. This reasoning brought us to the derivation of calibration TPs from Sentinel-1 data on the basis of PSI methodological theory, which, under specific circumstances, can be then used to anchor two single-pass subsequent TDX DEMs for mutual calibration and differencing purposes. In this article, we present the developed methodology and we discuss the different aspects that allow us to consider TP candidates selected from Sentinel-1 time-series also reliable when applied to TDX bistatic acquisitions for performing mutual calibration, having to cope with issues related to the different radar frequencies, resolutions and acquisition geometries of both missions.

The rest of this article is organized as follows. Section II describes the theoretical impact of baselines estimation on the retrieved DEM height, quantifying expected error ranges for TDX DEM pairs. Section III describes the proposed methodology and the necessary precalibration phase. Results and validation are presented in Section IV. Finally, Section V concludes this article.

II. Impact of Baseline Estimation Uncertainties on the Retrieved Height in TDX DEMs

Together with errors in InSAR DEMs caused by random noise contributions (i.e., the relative height error [20], [21]), one has

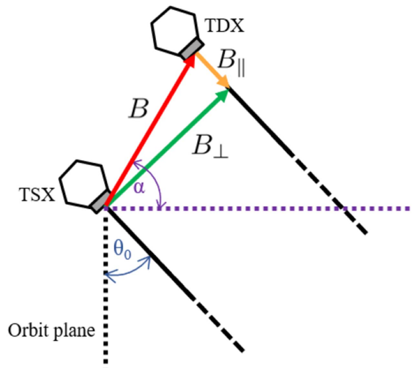

Fig. 2. Single-pass across-track InSAR geometry, comprising the TSX and TDX satellites. B represents the across-track baseline, while $B_{\perp}$ and $B_{\parallel}$ are the projections perpendicular and parallel to the line of sight, respectively.

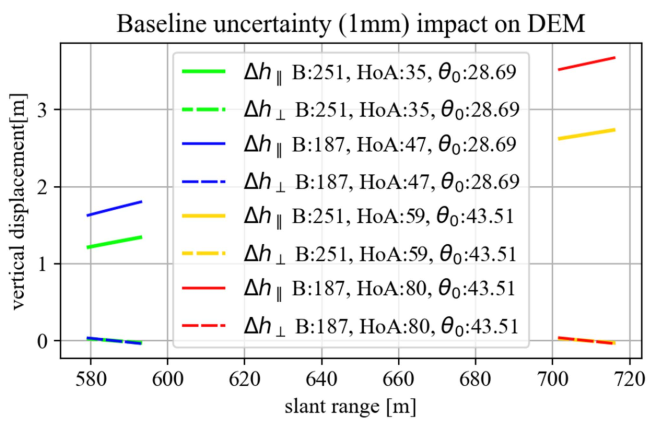

Fig. 3. Simulation of vertical displacement corresponding to a baseline uncertainty of 1 mm parallel to the line of sight and 1 mm perpendicular to the line of sight.

also to consider the finite accuracy in the estimation of the baseline B which reflects in its projections $B_{\perp}$ (perpendicular to the line of sight) and $B_{\parallel}$ (parallel to the line of sight) presented in Fig. 2. These types of error appear as low-varying offsets and tilts [3]. In particular, they can be divided into three main contributions: along-track, across-track, and radial uncertainties. The along-track uncertainty can be sufficiently mitigated during the coregistration process and are typically negligible. Differently, across-track and radial uncertainties may cause errors in both the line of sight ($\Delta B_{\parallel}$) and perpendicular to the line of sight ($\Delta B_{\perp}$). In the following, we recall the formulation of each contribution and we assess the impact in typical TDX-like scenarios. In this context, we consider that the TDX baseline calibration in bistatic configuration resulted in a standard deviation of 1 mm, fulfilling the mission requirement [9].

One of the main parameters which plays a crucial role in the assessment of DEM uncertainties is the height of ambiguity. This represents the topographic height corresponding to a complete 2π phase cycle of the interferometric phase and is defined for the single-pass InSAR case as [3]

$$h_{\text{amb}} = \frac{\lambda r \sin \theta_{\text{i}}}{B_{\perp}} \tag{1}$$

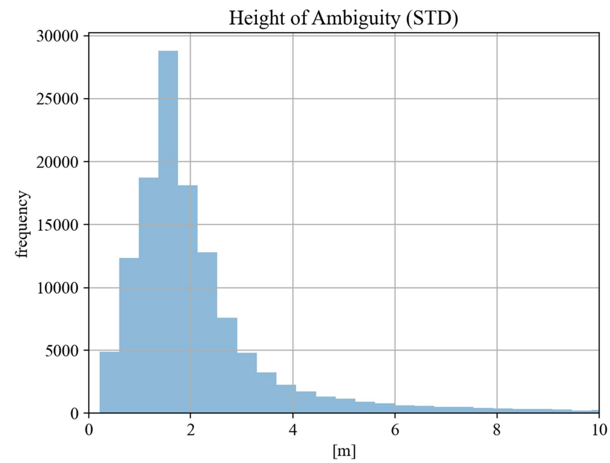

Fig. 4. Histogram of the height of ambiguity variation (STD) within TDX bistatic InSAR scenes.

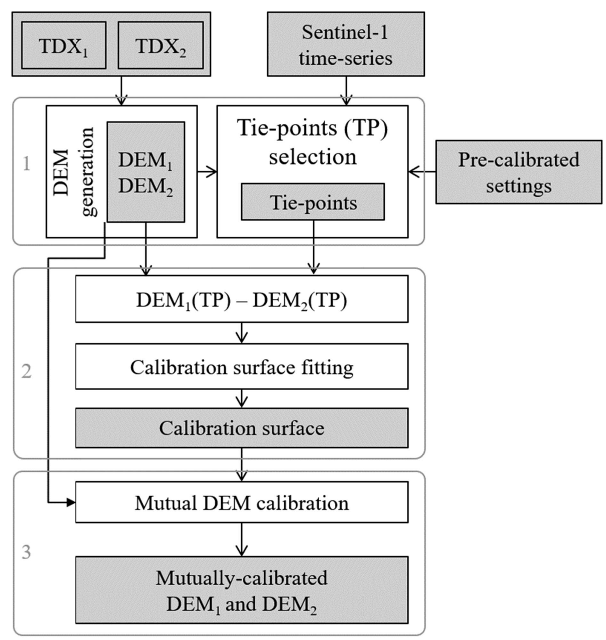

Fig. 5. High-level concept of the proposed algorithm for the Sentinel-1-aided mutual calibration of TDX DEMs. White blocks represent operations while gray boxes identify input, intermediate and output products.

where λ is the wavelength, r is the distance to the satellite or slant range, θ_{i} is the incidence angle, and $B_{\perp}$ is the baseline perpendicular to the line of sight.

Baseline uncertainties cause errors in the generated DEMs, affecting the estimated height. In particular, they result in a slant range variation $\delta_{\Delta R}$, calculated as the variation of the distance between the secondary satellite of the bistatic constellation (i.e., TDX in Fig. 2) and an illuminated target.

This is directly proportional to the height error Δh in the DEM through

$$\Delta h = \frac{h_{\text{amb}} \delta_{\Delta R}}{\lambda} = r \sin(\theta_{\text{i}}) \frac{\delta_{\Delta R}}{B_{\perp}}. \tag{2}$$

The vertical displacements are not only represented by a constant offset but also by a tilt resulting from the changes in slant range and incidence angle occurring within an acquisition. Moreover, baseline uncertainties can be decomposed into their components parallel and perpendicular to the line of sight, as detailed in the following.

A. Baseline Uncertainties Parallel to the Line of Sight

Uncertainties in the line of sight yield a variation in slant range $\delta_{\Delta R} = \Delta B_{\parallel}$ and the corresponding vertical displacement can be expressed as follows:

$$\Delta h_{\parallel} = r \sin(\theta_{\mathrm{i}}) \frac{\Delta B_{\parallel}}{B_{\perp}}. \tag{3}$$

If we consider a minimum $h_{\mathrm{amb}} = 35$ m with $\theta_0 = 30^{\circ}$ and a maximum $h_{\mathrm{amb}} = 80$ m with $\theta_0 = 43^{\circ}$, we can expect a vertical displacement in the DEM, which varies from about 1.32 m with a tilt of 0.16 m up to 3.64 m with a tilt of 0.38 m, respectively.

B. Baseline Uncertainties Perpendicular to the Line of Sight

The slant variation of the secondary satellite caused by a perturbation in the perpendicular baseline component can be quantified as follows:

$$\begin{aligned}\delta_{\Delta R} = &\left((x - B\cos(\alpha))^2 + (h_{\mathrm{sat}} + B\sin(\alpha))^2\right)^{\frac{1}{2}} \\ &- (x - B\cos(\alpha) - \Delta B_{\perp}\cos(\theta_0))^2 \\ &+ (h_{\mathrm{sat}} + B\sin(\alpha) + \Delta B_{\perp}\sin(\theta_0))^2 \frac{1}{2}\end{aligned} \tag{4}$$

where x is the ground range, h_{sat} is the satellite height, θ_0 is the angle in the line of sight, and α is the relative angle between the two satellites (radial component, with impact below mm).

If we consider a minimum $h_{\mathrm{amb}} = 35$ m with $\theta_0 = 30^{\circ}$ and a maximum $h_{\mathrm{amb}} = 80$ m with $\theta_0 = 43^{\circ}$, we can expect a vertical tilts in the DEM which vary from to 0.07 m up to 0.19 m, respectively.

C. Combination of Errors in DEM Differentiation

The overall expected Δh components for a near-range and far-range TDX beam are depicted in Fig. 3, by considering a best and worst case scenario characterized by h_{amb} between 35 and 80 m, respectively. In conclusion, regarding the TDX mission, uncertainties in the baseline component parallel to the line of sight have a predominant impact on the vertical displacement with respect to uncertainties perpendicular to the line of sight, yielding offsets of the order of several meters. Nevertheless, both components result in DEM tilts along the swath of comparable magnitude. Moreover, when we consider an entire DEM scene, it is important to point out that the height of ambiguity (and, therefore, the baseline) also varies depending on the orbit formation. This results in an overall azimuth-/range-dependent vertical displacement. Typical values of Δh_{amb} are depicted in Fig. 4, which shows the histogram of the height of ambiguity variations within all bistatic InSAR scenes acquired during the TDX mission. In fact, if we consider possible Δh_{amb} variations between 0.3 m and 10 m, this leads to variations in the vertical displacement between 1 and 32 cm, respectively.

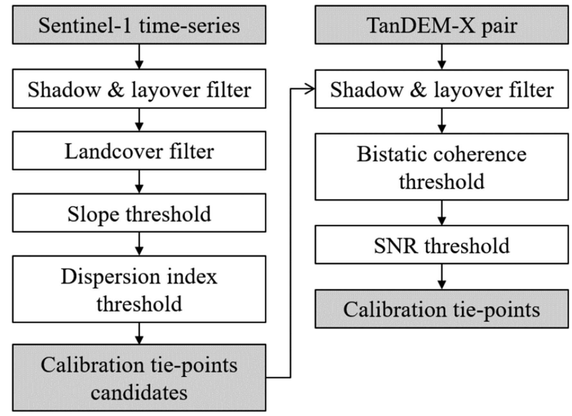

Fig. 6. Complete flowchart for the selection of suitable calibration TPs.

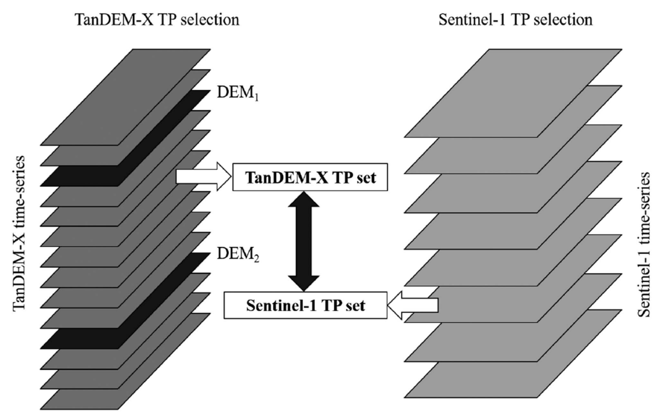

Fig. 7. Algorithm precalibration scheme for the selection of a suitable threshold on the Sentinel-1 amplitude dispersion index.

Moreover, when differentiating two overlapping DEMs, one has to be aware that the above-mentioned offsets and tilts sum up in an either constructive or destructive way depending on the sign of the error. This corresponds to a low-varying vertical displacement that needs to be properly estimated and compensated for before DEM differentiation. In light of the numerical examples presented previously and considering a worst-case scenario where errors constructively sum up when considering an uncalibrated overlapping TDX DEM pair, one can expect absolute vertical displacements on the order of a few cm up to about 5 m and relative low-varying vertical displacements in range and azimuth up to about 1.5 m.

III. Methodology

The flowchart in Fig. 5 presents the high-level concept of the proposed algorithm. Given the availability of two time-tagged TDX bistatic acquisitions (TDX_1 and TDX_2) and their respective DEMs (DEM_1 and DEM_2) the first step concerns the selection of suitable calibration TPs by combining Sentinel-1 interferometric time-series, TDX SAR, and InSAR-derived quantities and precalibrated settings. The second step refers to

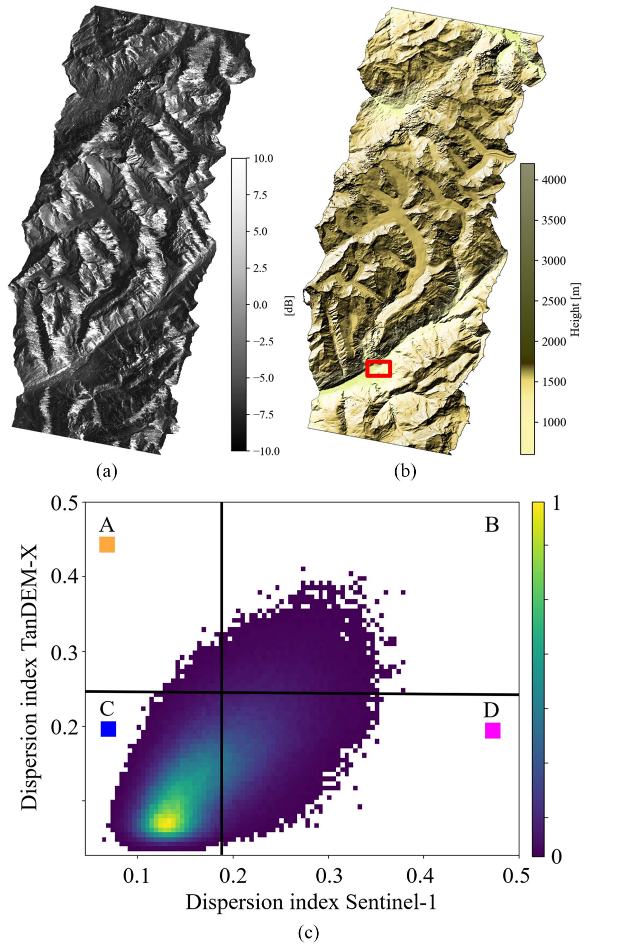

Fig. 8. (a) Multitemporal average backscatter of a TDX bistatic time-series surrounding the Aletsch Glacier, CH. (b) Exemplary DEM (color hill-shade) from a single bistatic acquisition of the considered time-series. The red square identifies the area depicted in Fig. 9. (c) 2-D normalized histogram of the amplitude dispersion index $\mathcal{D}_A$ for C-band Sentinel-1 (on the horizontal axis) and X-band TDX (on the vertical axis).

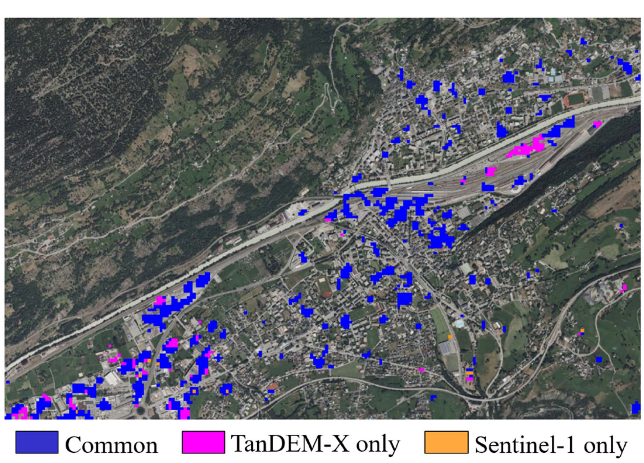

Fig. 9. Example of TPC for the considered precalibration scenario. The depicted area corresponds to the red square in Fig. 8(b). The different colors correspond to values in the quadrants A, C, and D in Fig. 8(c): Common TPC to both TDX and Sentinel-1 (blue, quadrant C), TPC detected in the considered TDX time-series only (pink, quadrant D), and TPC detected in the Sentinel-1 a time series only (orange, quadrant A), respectively. The TPC are superimposed to an optical image from GoogleEarth.

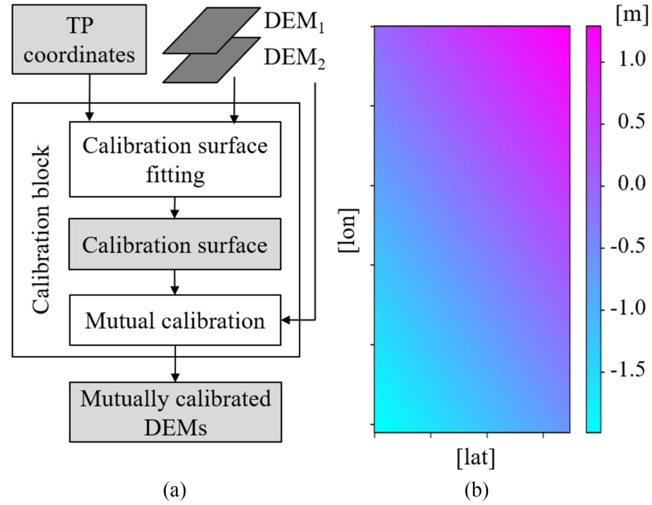

Fig. 10. (a) Flowchart for the estimation of the calibration surface and final mutual calibration of TDX DEMs. (b) Example of fitted calibration surface.

the estimation of a proper calibration surface, fitted to minimize the difference between DEM_1 and DEM_2 over the selected TPs. Finally, the last step consists in the proper mutual calibration of two DEMs.

A. Selection of Calibration TPs

In order to be used for mutual DEM calibration, natural targets need to be characterized by a high stability in time within the time interval between the two time-tagged DEMs and to assure a good quality on the corresponding DEMs. These aspects translate in the requirement of selecting highly coherent scatterers.

The flowchart for the selection of suitable calibration TPs is presented in Fig. 6. Here, we first consider a time-series of co-registered Sentinel-1 images covering the same area of the TDX DEMs to be mutually calibrated. Regions affected by geometric distortions, such as shadow and layover, caused by the side-looking nature of SAR, are discarded, as well as with pixels classified as permanent snow and ice within an external reference land cover map (for the results in Section IV we consider the Copernicus Land Cover Map [22]). This second aspect is necessary to avoid the selection of calibration targets which might show a relatively high coherence but whose topographic height might be affected by penetration effects of the radar waves into the snow pack [23], [24], [25]. Moreover, we only consider pixels characterized by the presence of low-relief local topography, by setting a threshold at 10° on the predominant local slope, evaluated by computing the 2-D gradient of an external reference DEM (such as, e.g., the global TDX edited DEM [6]). This step is important to avoid the use of TPs affected by inaccuracies caused by residual errors during the interpolation of the DEMs on the same output grid (especially over high-relief terrain).

Afterward, we select calibration tie-point candidates (TPCs) from the time-series of Sentinel-1 data on the basis of classical PSI methodology [26], [27]. In particular, persistent (or permanent) scatterers are stable natural reflectors which can be isolated from long co-registered temporal series of InSAR images,

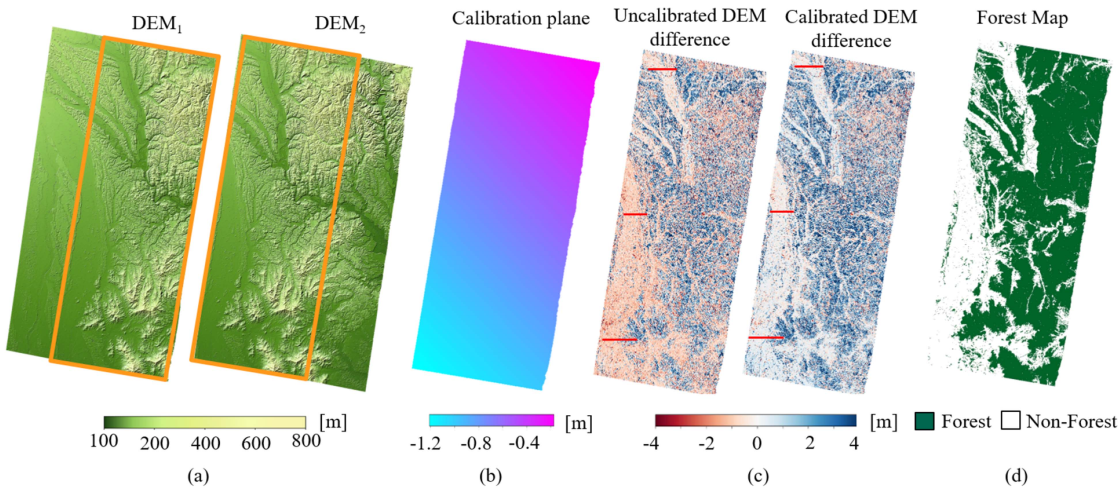

Fig. 11. Example of mutual DEM calibration using two time-tagged TDX DEMs over Japan (DEM$_1$ AID: 1705863, DEM$_2$ AID: 1521912). From left-to-right, (a) shows the two input DEMs as colored hill shade image, (b) the calibration surface, (c) the uncalibrated DEM difference (left) and the mutually calibrated DEM difference (right) of the overlapping areas identified by the orange boxes in (a), and (d) the corresponding forest/non-forest map, generated using the algorithm in [28]. The red lines in (c) identify two transects which are depicted in Fig. 13.

by exploiting their high temporal and geometrical coherence, and by compensating for atmospheric variations. Typically, a time-series with at least 20 images has to be considered, to allow for the reliable selection of persistent scatterers (PS), by considering their temporal stability. In particular, the first step of the proposed procedure in [26] consists in identifying possible persistent scatterers candidates (PSC) by setting a threshold on an amplitude dispersion index $\mathcal{D}_A$, defined as follows:

$$\mathcal{D}_A = \frac{\sigma}{\mu} \tag{5}$$

where for each pixel of the co-registered InSAR time-series, μ represents the temporal mean value of the amplitude and σ the corresponding standard deviation. Targets are considered to be stable in amplitude for values of $\mathcal{D}_A$ lower than a certain threshold. In our case, the optimal value of this threshold is selected during an algorithm precalibration phase which allows for minimizing false alarms between scattering responses acquired by two different sensors, i.e., Sentinel-1 and TDX. The reasoning behind the threshold selection is presented later on in Section III-B.

Moreover, it was demonstrated in [26] that, in addition to amplitude stability, low values of $\mathcal{D}_A$ are also a good approximation of phase stability in presence of high signal-to-noise ratio (SNR). This condition is of crucial importance and it is considered later on when setting proper thresholds on TDX data.

At this point, a set of calibration TPCs, derived from Sentinel-1 repeat-pass data, is available. This needs to be further refined in order to get calibration TP that are appropriate for the mutual calibration of single-pass TDX DEMs. For this purpose, we now consider the pair of bistatic TDX acquisitions, from which the two DEMs to be mutually calibrated are derived. First of all, regions affected by shadow and layover are filtered out, as already done for the Sentinel-1 acquisition geometry. This step assures that no selected targets are affected by geometric distortions in both Sentinel-1 and TDX data. Then, a threshold is set on the bistatic InSAR coherence of both TDX bistatic acquisitions, in order to assure a good quality of the TDX DEM in correspondence of the selected calibration TP. For the specific case of TDX, we selected a quite conservative coherence threshold value of 0.7. Indeed, the coherence is defined as the absolute value of the normalized cross-correlation coefficient between the interferometric image pair as follows:

$$\gamma_{\text{tot}} = \frac{|E[u_1 u_2]|}{\sqrt{E[|u_1|^2 |u_2^*|^2]}} \tag{6}$$

where u_1 and u_2 represent the primary and secondary images, E is the expectation value and $*$ is the complex conjugate operator. γ_{tot} quantifies the amount of noise in the interferogram and represents therefore the key quantity for assessing the quality of the generated DEM. Note that the spatial coherence is not sufficient per se for assuring the selection of reliable TPs (skipping the TPC set estimation). Indeed, if we only considered the spatial coherence of the two TDX DEMs, the risk would be to include targets affected by temporal changes as TPs. One could think about an urban scenario, an open-pit mine, or even a volcanic eruption. In all these cases, a target could be highly coherent in the first DEM, then change, and then appear highly coherent again in the second DEM. For this reason, a condition on the temporal stability of the target is necessary to drastically reduce the probability of including these kinds of targets in the mutual calibration process.

Finally, a further threshold is applied on the SNR of both TDX bistatic acquisitions, in order to assure the selection of stable natural targets with respect to the phase, as phase stability is assured by amplitude stability in presence of high SNR [26]. The SNR is computed as follows:

$$\text{SNR} = \frac{\beta^0 - \beta^n}{\beta^n} \tag{7}$$

where β^0 identifies the temporal mean radar brightness and β^n is the temporal mean of the noise equivalent β^0, which

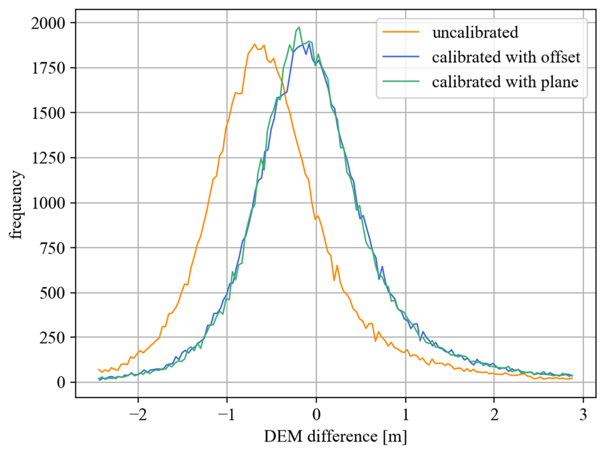

(a)

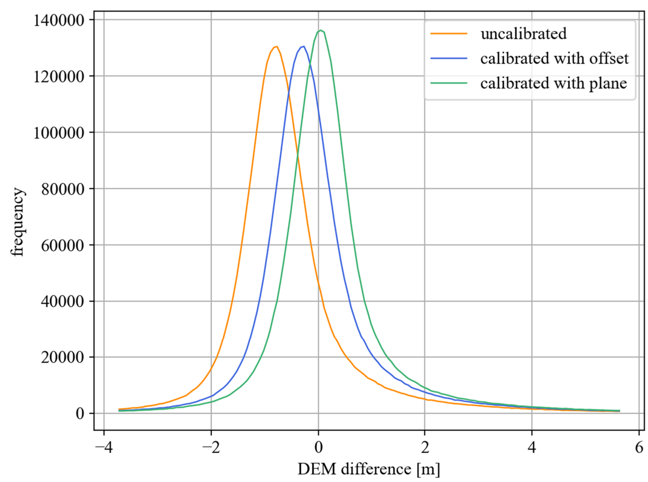

(b)

Fig. 12. (a) Histograms of the noncalibrated and calibrated DEM difference with a plane and offset for the TPs. (b) Histograms of the noncalibrated and calibrated DEM difference with a plane and offset for nonvegetated areas, masked out using the TDX-derived forest/non-forest map depicted in Fig. 11(d).

represents the system noise floor. In order to ensure that this second condition holds, we constrained the selection of valid TPs to those pixels where the SNR is higher than a certain threshold. Moreover, this condition allows us to significantly simplify the procedure for the selection of stable TPs with respect to classical PS selection, since it is based on the selection of PSC only and does not require for the computation of the temporal coherence. Also in this case, considerations on the proper setting of the SNR threshold are drawn in Section III-B.

Finally, it is important to consider that the accuracy of the proposed method is impacted, on the one hand, by the spatial distribution of the TPs for the regression of the calibration surface, and, on the other hand, by the overall number of available TPs. Indeed, an adequate spatial distribution on the horizontal plane of the TPs reduces potential biases in the estimation of the calibration surface, while the number of TPs impacts the robustness of the method, since it mitigates the impact of random noise in the data (i.e., the relative height accuracy [20], [21]) and reduces the effects of remaining outliers.

B. Thresholds Precalibration Procedure

a) Threshold on the amplitude dispersion index $\mathcal{D}_A$: The most crucial aspect of the proposed algorithm is to ensure that the TPC, a section of the PSC, derived from Sentinel-1 time-series at C-band under the above-mentioned conditions, are also suitable TPs for the mutual calibration of TDX DEMs, derived from bistatic data at X-band and with different acquisition geometries with respect to Sentinel-1. To this purpose, we focus on the specification of proper settings which allow for achieving a good compatibility between Sentinel-1 and TDX data. Indeed, when considering SAR sensors at different frequencies, a different behavior in terms of backscatter levels, as well as interferometric performance, i.e., coherence, is expected.

The precalibration procedure hereby described refers to the empirical approach developed for setting a proper threshold on the amplitude stability index $\mathcal{D}_A$, computed from the Sentinel-1 time-series, which can assure the selection of stable natural targets when considering the same area acquired with TDX bistatic acquisitions. For this purpose, we selected a dedicated precalibration test site, where a Sentinel-1 InSAR time-series and a TDX InSAR time-series are available. Both time-series must be accurately co-registered and referred to the same coordinates system and spatial grid (see Fig. 7). Specifically, we chose two time-series surrounding the Aletsch Glacier in Switzerland, which are characterized by the presence of different kinds of terrain, ranging from steep mountains to flat valley floors, from vegetated areas to snow/ice covered ones or to bare soil. The multitemporal mean backscatter of the considered TDX time-series and an exemplary DEM generated from a single bistatic InSAR acquisition are depicted in Fig. 8(a) and (b), respectively. After the application of the first three filtering steps presented on the left-hand column of Fig. 6, the amplitude stability index $\mathcal{D}_A$ can be computed for both time-series using (5). We select all reasonably stable values in both time-series characterized by $\mathcal{D}_A \in [0, \ldots, 0.5]$ for computing the 2-D normalized histogram of $\mathcal{D}_A$, as in Fig. 8(c). Here, the shift of the histogram from the bisector of the quadrant is related to the different responses of the targets when illuminated by either TDX or Sentinel-1, caused by different acquisition geometries as well as different radar frequencies. By setting a certain threshold on $\mathcal{D}_A$ for each of the considered sensors (horizontal and vertical black lines for Sentinel-1 and TDX, respectively), the 2-D space of the histogram can be divided into four quadrants: A—TPC selected only in Sentinel-1 data, B—discarded targets in both time-series, C—common TPC, D—targets selected only in TDX data. Once a satisfying threshold value on $\mathcal{D}_A$ is selected *a priori* for the TDX data (in this case we set it at 0.25) assuring a good stability of the selected targets, the optimal threshold for Sentinel-1 is then chosen as a tradeoff between assuring a good stability of the selected targets and minimizing false positives candidates with respect to TDX. False alarms correspond to targets selected in Sentinel-1 data, which do not satisfy the stability requirement in TDX data (quadrant A), while the selected targets are the common TPC (quadrant C). For the considered precalibration scenario, setting a threshold on the TDX $\mathcal{D}_A$ at the maximum value of 0.25, as proposed in the literature [26], and considering

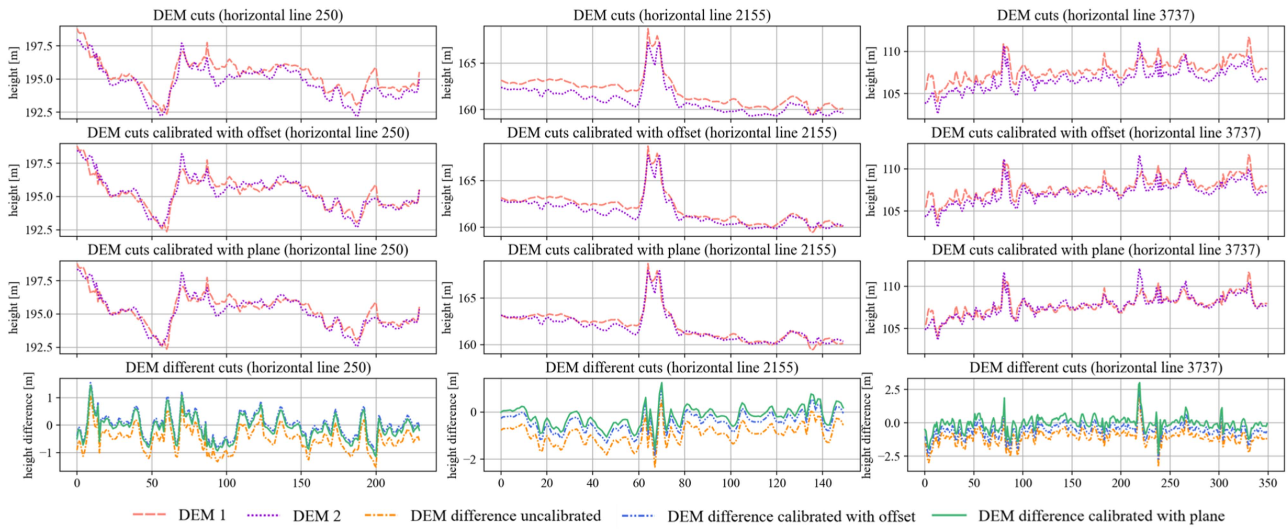

Fig. 13. DEM_1 DEM_2 and DEM difference for the red transects in Fig. 11(c). Each column refers to a different transect: Top row—transect without calibration, second row—transect with calibration considering an offset, third row—transect with application of the proposed DEM mutual-calibration algorithm with a plane, bottom row—DEM difference considering the transects previously.

an acceptable rate of false alarms equal to 1% of all considered targets results in a maximum threshold value on the Sentinel-1 $\mathcal{D}_A$ of 0.19. An example of TPC for the considered precalibration scenario is presented in Fig. 9. The depicted area corresponds to the red square in Fig. 8(b). The different colors correspond to values in the quadrants A, C, and D in Fig. 8(c): common TPC to both TDX and Sentinel-1 (blue, quadrant C), TPC detected in the considered TDX time-series only (pink, quadrant D), and TPC detected in the Sentinel-a time series only (orange, quadrant A), respectively. Overall, over this area, only few TPC belonging to Sentinel-1 only are present, which ensures a good match with the TDX data.

b) Threshold on the SNR: From PSI theory, the threshold on the SNR should be set on the temporal mean of the SNR of the entire time-series of PSC, in order to assure a high-temporal coherence. It is important to highlight again that, even if TPC are selected as a subset of PSC from Sentinel-1 time-series, such a threshold needs to be applied to TDX SNR values, in order to assure high stability of the selected calibration TPs in the TDX DEM acquisitions. From the literature, the overall minimum SNR to be consider is 4 dB [26], nevertheless we empirically set a more conservative target SNR value to be over 12 dB with a minimum of 1% of TPCs. One should be aware that a lower value could also be chosen depending on the scenario and the distribution of TPs within the considered scene.

C. Estimation of the Calibration Surface and Mutual DEM Calibration

The overall concept for performing mutual DEM calibration is presented in Fig. 10(a). Once the calibration TPs are selected, the corresponding TDX DEMs values from both acquisitions (DEM_1 and DEM_2) to be calibrated are used to estimate the calibration surface. First of all, the difference Δ between DEM_1 and DEM_2 over the selected calibration TPs is evaluated as

TABLE I
ESTIMATED ACCUMULATED BULK LAVA VOLUMES IN MILLIONS OF M^3 FOR THE CONSIDERED ERUPTIONS OCCURRED IN THE REYKJANES PENINSULA, ICELAND, BETWEEN 2021 AND 2023 WITHOUT MUTUAL CALIBRATION OF TDX DEMS (SECOND COLUMN), BY CALIBRATING WITH AN OFFSET ONLY (THIRD COLUMN) AND BY APPLYING THE PROPOSED DEM CALIBRATION TECHNIQUE (FOURTH COLUMN)

Estimated Bulk Lava Volumes [10^6 m^3]				
Eruption	DEM difference without calibration	DEM difference offset calibrated	DEM difference mutually calibrated	Photogrammetric reference
2021—six months 19.03–18.09 Fagradalsfjall	143.8	146.5	146.3	150 ∓ 3
2022—18 days 03.08–21.08 Fagradalsfjall	11.8	10.4	11.3	11 ∓ 0.4
2023—26 days 10.06–05.08 Fagradalsfjall	12.4	15.5	15.6	15
2023—three days 18.12–21.12 Svartsengi	8.7	10.6	11.1	11

Reference valued derived from aerial photogrammetric DEMs are reported in the last column [29].

follows:

$$\Delta(\mathrm{TP}) = \mathrm{DEM}_1(\mathrm{TP}) - \mathrm{DEM}_2(\mathrm{TP}). \quad (8)$$

A defined calibration surface Δ_{Cal} can now be fitted to the $\Delta(\mathrm{TP})$ values. As surface we consider a plane and as fitting method the least squares. Higher order polynomial surfaces were also considered during the method design phase. Since they did not bring any significant improvement in the calibration performance, we selected a plane as a good compromise between final accuracy and computational load. One should note that, in order to perform the fitting, the spatial location of the considered DEMs values has clearly to be preserved. An example of calibration surface is presented in Fig. 10(b).

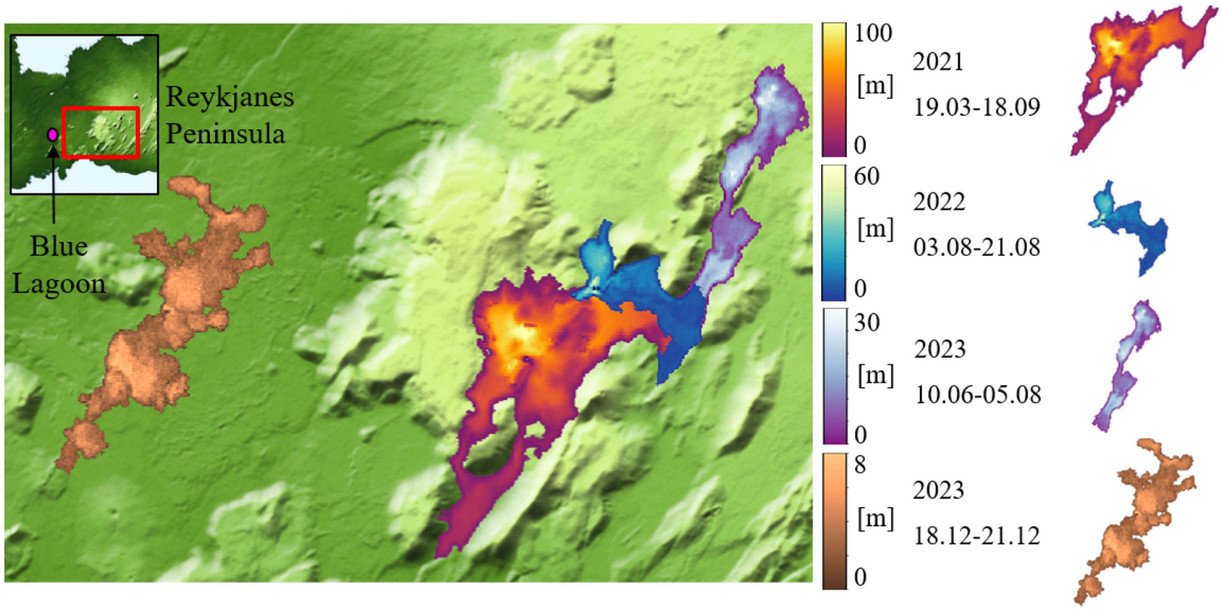

Fig. 14. Lava accumulation thickness maps of the four eruptions in the Reykjanes Peninsula, Iceland between 2021 and 2023. The zoom-in in the top-left corner shows a detail of the TDX global DEM for the considered area (red square) in the Reykjanes Peninsula and the location of the Blue Lagoon geothermic area.

Let us now assume that DEM_1 represents the reference DEM and DEM_2 the one that has to be calibrated with respect to DEM_1. Δ_{Cal} is then used to perform the mutual DEM calibration by calibrating DEM_2 with respect to DEM_1 as follows:

$$DEM_2^{Cal} = DEM_2 + \Delta_{Cal}. \tag{9}$$

By doing so, DEM_1 and DEM_2^{Cal} are now properly mutually calibrated and can be correctly used for applications based on DEM differentiation.

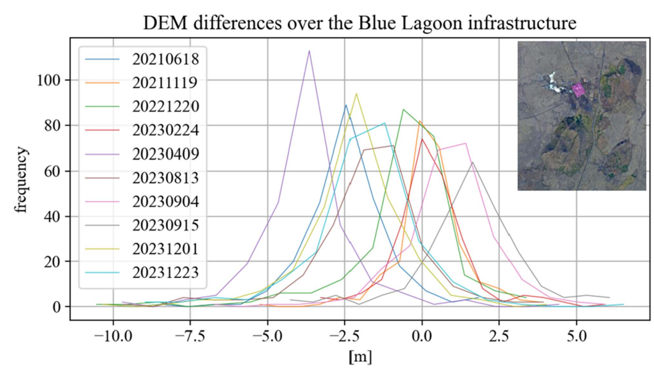

Fig. 15. TDX DEM differences with respect to the first reference acquisition over the infrastructure of the Blue Lagoon for the estimation of the calibration offset. The zoom-in on the top-right shows in pink the area used to estimate the offset.

IV. Results

A. DEM Mutual Calibration

A first example of TDX DEMs mutual calibration is presented in Fig. 11. Here, we consider two overlapping single-scene DEMs acquired over Japan [see Fig. 11(a), DEM_1: acquisition date 2020.04.04, Acquisition ID (AID) 1705863; DEM_2 : acquisition date 2018.08.19 and AID 1521912]. The calibration surface, estimated by considering the overlapping area identified by the orange boxes in Fig. 11(a), is depicted in Fig. 11(b), while the DEM differences, without (left) and with (right) the application of the proposed mutual calibration algorithm, respectively, are displayed in Fig. 11(c). One can note that several extended areas present residual differences in the order of 2–4 m. These regions are characterized by the presence of vegetation, as visible from the corresponding forest/nonforest map depicted in Fig. 11(d), which is derived from the interferometric coherence of the first acquisition (DEM_1) by applying the classification method published in [28]. Consequently, since the TDX DEMs were acquired at different seasons (DEM_1 at the beginning of spring and DEM_2 in midsummer), we expect the vegetation to show different kinds of interactions with the illuminating radar waves (leaf-on versus leaf-off condition). This yields different amounts of penetration of the radar waves into the canopy and, subsequently, to different vertical locations of the mean radar phase center within the vegetation vertical profile. Differently, the DEM difference maps over nonvegetated areas show residual offsets in the order of about –1 m in the uncalibrated DEM difference, while these effects are almost negligible in the calibrated one. This is clearly visible when considering the histograms in Fig. 12 and the transects in Fig. 13. In this example we consider two variants of calibration surface: offset, where the same calibration value is applied to the whole scene, and plane, which also considers possible tilts. In Fig. 12 the histograms of the DEM difference for the TPs (a) and the nonforested areas (b) are shown considering the uncalibrated DEM pair (orange), the mutually calibrated DEM pair with an offset (blue) and the mutually calibrated DEM pair with the proposed technique (green). One

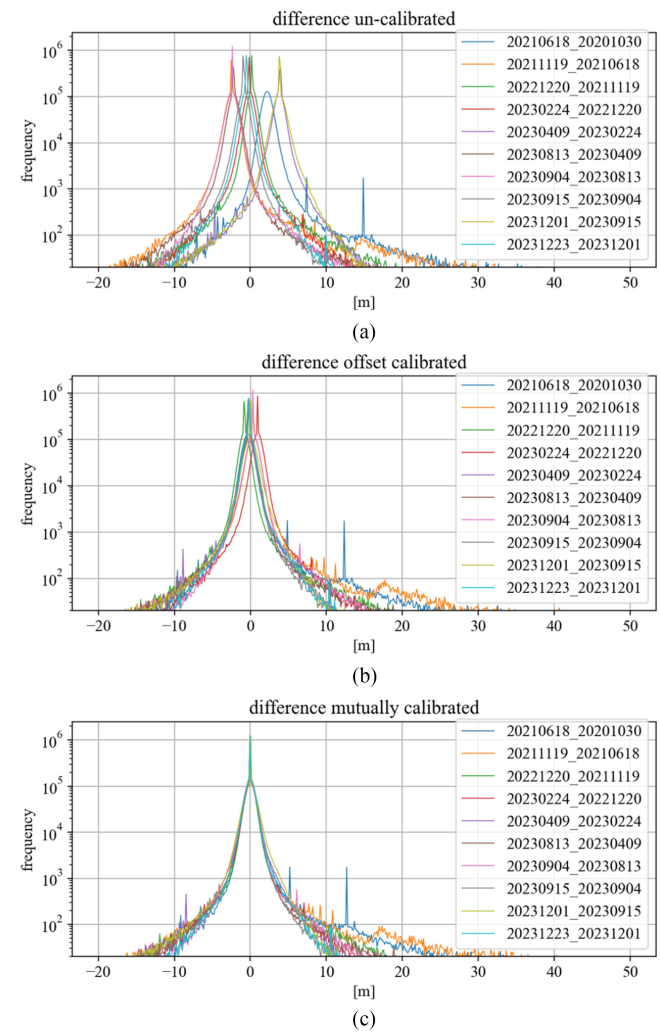

Fig. 16. Histograms of the DEM differences (in logarithmic scale) with respect to the reference DEM for all the considered TDX acquisitions over Iceland. (a) Without any mutual calibration, (b) with offset compensation only, and (c) with the proposed mutual calibration.

should note that, in this particular case, we estimated the offset as the mean height of all TPC detected within the scene. This approach was necessary due to the fact that no external reference GPS or LiDAR measurement was available. As it can be seen, the DEM difference calibrated using the proposed approach (green) achieves the best performance, showing insignificant remaining bias and the lowest standard deviation. The latter is confirmed by the highest peak of the green distribution, given the exact same number of input pixels for all different histograms. The DEM transects in Fig. 13 correspond to the red lines in Fig. 11(c). Each column of the figure corresponds to a different transect, while the rows show, from top to bottom, the pair of DEMs without mutual calibration, calibrated with an offset only, and calibrated with the proposed technique, respectively. The plots at the bottom of Fig. 13 depict the DEM difference for all the considered calibration scenarios. Here, the impact of a precise mutual calibration can be appreciated, with the uncalibrated DEM difference (orange) and the proposed calibration technique (green) resulting in the highest and lowest remaining bias, respectively.

B. *Lava Fields Volume Estimation*

The proposed mutual calibration of single-scene TDX DEMs can be utilized for precisely measuring height and volume changes in time. An example is the monitoring of lava fields, which build up during a volcanic eruption. Four different eruptions in the Reykjanes Peninsula, Iceland, took place between 2021 and 2023. Three of them concern the Fagradalsfjall volcanic system, occurring in 2021 (03.19–09.18), 2022 (08.03–08.21), and 2023 (06.10–08.05), and the last one belonging to the Svartsengi volcanic system in 2023 (12.18–12.21) [29]. We consider a set of 11 TDX DEMs derived from acquisitions with different InSAR geometries, covering a time span from 2020.10.30 up to 2023.12.23, with at least one DEM acquired prior to and one after each of the eruptions.[1]

We selected the first DEM from 2020.10.30 as reference DEM and calibrate all other ten DEMs to this reference with the proposed technique. Fig. 14 shows the estimated lava thickness maps of newly formed lava fields for each considered eruptions, superimposed to the reference TDX DEM (in green hillshade scale). For comparison purposes, we also consider the same DEMs with no *a priori* mutual calibration and calibrated with a pure offset only with respect to the reference DEM, equivalent to the method considered in [11]. The offset is derived in this case by considering the mean elevation difference between overlapping DEMs in correspondence of the infrastructures to the Blue Lagoon geothermal area (centered around 63°52’49.05”N latitude, 22° 26’52.13”W longitude, between 3 and 10 km west from the eruption sites), which is the closest manmade settlement to the eruption fields and common to all TDX acquisitions. Fig. 15 shows the DEM difference histograms over the considered area and its location.

The results of the estimated bulk lava volumes for all different calibration techniques are summarized in Table I. As reference values for validation, in the last column we report the bulk lava volumes for the considered eruptions obtained with nearly real-time photogrammetric aerial DEMs [29]. A good agreement can be found between the photogrammetric data and the estimated bulk lava volumes obtained after applying the proposed mutual calibration technique (**DEM difference mutually calibrated** column), with an overall mean difference of only 1.3%, corresponding to a lava volume of about 1.3 million m^3. A slightly higher mean offset of 2.4% is present when calibrating with an offset only (**DEM difference offset calibrated** column), yielding an error of 1.6 million m^3. Finally, the estimation without performing the mutual calibration at all leads to an error in the order between 1.7% and 21.6% of the total volume, which corresponds to 8.4 million m^3.

[1] The exact acquisition dates and AIDs (in brackets) of the considered TDX DEMs are: 2020.10.30 (1757314), 2021.06.18 (1826269), 2021.11.19 (1839959), 2022.12.20 (1976545), 2023.02.24 (2004130), 2023.04.09 (2024202), 2023.08.13 (2048610), 2023.09.04 (2044261), 2023.09.15 (2044268), 2023.12.01 (2078074), 2023.12.23 (2085545)

Finally, Fig. 16 depicts the histograms of the computed DEM differences (in logarithmic scale) with respect to the reference DEM (oldest acquisition) for all the considered TDX DEMs over Iceland. From top to bottom, they are evaluated without any mutual calibration, with offset compensation only and by applying the proposed mutual calibration, respectively. One can appreciate that no residual bias is visible after the application of the proposed mutual calibration algorithm, as the histogram peaks are correctly aligned, which is not the case when calibration is performed by simply correcting for a single offset. Interestingly, the histogram tails spotted up to about 30 m are caused by the accumulation of new lava volumes. Moreover, one should note that the histograms are not normalized and that the total numbers of pixels correspond to the different overlaps between the acquisitions.

V. Conclusion

In this article, we presented a novel approach for a precise mutual-calibration of DEMs derived using across-track SAR interferometry. Specifically, we considered the calibration of time-tagged TDX DEMs by solely relying on natural calibration targets derived from PSC using Sentinel-1 data, as well as from additional considerations on the InSAR acquisition geometry, radar frequency and scene characteristics. The algorithm delivers highly accurate results at the advantage of a limited computational complexity. Indeed, the use of sole PSC, selected on the basis of the amplitude dispersion index, and the additional constraints on the SNR and the spatial coherence allow for the selection of reliable natural calibration targets, without the need, e.g., for implementing an entire PSI processing chain. This should also allow users from diverse communities, who are not particularly familiar with the details of PSI processing, to properly perform a mutual calibration of single-pass InSAR DEMs for their higher level scientific applications. Interestingly, the method can also be applied to other sensors operating at different frequencies, by simply performing a dedicated thresholds pre-calibration procedure. Moreover, it is also worth mentioning that no recalibration of the algorithm setting is normally necessary when considering the same sensors (i.e., TDX and Sentinel-1) over different scenarios. This was demonstrated by the real-case validation performed over Iceland, since the algorithm settings were derived using a test site surrounding the Aletsch Glacier in the Swiss Alps and no changes were applied to the Iceland scenario. Nevertheless, we plan to further validate this aspect in the future by considering additional test sites characterized by different land cover, topography, and acquisition geometries. The proposed approach can be completely automatized and does not require the availability of external reference measurements, such as GPS data, being well suited for large-scale deployment or application over remote scenarios where the acquisition of reference measurements might be unfeasible. Moreover, we analyzed the importance of a precise mutual calibration of DEMs prior to differentiation for the quantification of height and volume changes, which, if not correctly performed, could lead to the presence of nonnegligible errors in the downstream applications. We demonstrated the effectiveness of the proposed methodology by considering as test-case scenario the estimation of new lava fields volumes from the volcanic eruptions occurred in the Reykjanes Peninsula, Iceland, between 2021 and 2023. The obtained results showed a very good agreement with reference high-resolution measurements obtained from aerial photogrammetric DEMs, with an overall mean estimation difference of only 1.3%. In light of these findings, it becomes apparent how a mutual DEM calibration based on offset compensation only is not sufficient for a precise estimation of height and volume changes through DEM differentiation. This aspect clearly impacts a large variety of downstream scientific applications and should be carefully considered.

Finally, it is important to mention that in this work we strictly considered scenarios, which are not affected by severe penetration effects of the radar waves into volumetric targets, such as, e.g., vegetation or snow and ice-covered areas. In these cases, the correct compensation for the elevation bias caused by penetration is of crucial importance to retrieve the height of the surface and to correctly perform DEM differencing, as this strongly impacts possible subsequential applications such as glacier mass balance and seasonal snow height retrieval. This aspect will be addressed in future works.

Acknowledgment

The technique is under patent protection [30]. The authors would like to thank the DLR colleagues who commanded the TanDEM-X acquisitions over Grindavík, together with the colleagues at the National Land Survey of Iceland, the Icelandic Institute of Natural History and the Icelandic Meteorological Office and Gianfranco Fornaro from IREA-CNR for the fruitful discussions.

References

[1] R. Bamler and P. Hartl, "Synthetic aperture radar interferometry," *Inverse Problems*, vol. 14, no. 4, pp. R1–R54, 1998.

[2] H. Zebker and J. Villasenor, "Decorrelation in interferometric radar echoes," *IEEE Trans. Geosci. Remote Sens.*, vol. 30, no. 5, pp. 950–959, Sep. 1992.

[3] G. Krieger et al., "TanDEM-X: A satellite formation for high-resolution SAR interferometry," *IEEE Trans. Geosci. Remote Sens.*, vol. 45, no. 11, pp. 3317–3341, Nov. 2007.

[4] M. Zink et al., "TanDEM-X: 10 years of formation flying bistatic SAR interferometry," *IEEE J. Sel. Topics Appl. Earth Observ. Remote Sens.*, vol. 14, pp. 3546–3565, 2021.

[5] P. Rizzoli et al., "Generation and performance assessment of the global TanDEM-X digital elevation model," *ISPRS J. Photogrammetry Remote Sens.*, vol. 132, pp. 119–139, Oct. 2017.

[6] C. Gonzalez, M. Bachmann, J. Bueso-Bello, P. Rizzoli, and M. Zink, "A fully automatic algorithm for editing the TanDEM-X global DEM," *Remote Sens.*, vol. 12, no. 23, Dec. 2020, Art. no. 3961.

[7] A. Gruber, B. Wessel, M. Huber, and A. Roth, "Operational TanDEM-X DEM calibration and first validation result," *ISPRS J. Photogrammetry Remote Sens.*, vol. 73, pp. 39–49, 2012.

[8] M. Lachaise, M. Bachmann, T. Fritz, M. Huber, B. Schweisshelm, and B. Wessel, "The TanDEM-X change DEM: The new temporal dem of the TanDEM-X mission," in *Proc. EUSAR 2021; 13th Eur. Conf. Synthetic Aperture Radar*, 2021, pp. 1–6.

[9] J. H. Gonzalez, M. Bachmann, G. Krieger, and H. Fiedler, "Development of the TanDEM-X calibration concept: Analysis of systematic errors," *IEEE Trans. Geosci. Remote Sens.*, vol. 48, no. 2, pp. 716–726, Feb. 2010.

[10] J. Kubanek, M. P. Poland, and J. Biggs, "Applications of bistatic radar to volcano topography - a review of ten years of TanDEM-X," *IEEE J.*

Sel. Topics Appl. Earth Observ. Remote Sens., vol. 14, pp. 3282–3302, 2021.

[11] S. Plank et al., “Combining thermal, tri-stereo optical and bi-static InSAR satellite imagery for lava volume estimates: The 2021 cumbre vieja eruption, La Palma,” *Sci. Rep.*, vol. 13, 2023, Art. no. 2057.

[12] J. Neelmeijer, M. Motagh, and B. Brookhagen, “High-resolution digital elevation models from single-pass TanDEM-X interferometry over mountainous regions: A case study of Inylchek glacier, central asia,” *ISPRS J. Photogrammetry Remote Sens.*, vol. 130, pp. 108–121, 2017.

[13] M. H. Braun et al., “Constraining glacier elevation and mass changes in South America,” *Nat. Climate Change*, vol. 9, pp. 130–136, 2019.

[14] J. Li et al., “Investigating the bias of TanDEM-X digital elevation models of glaciers on the Tibetan plateau: Impacting factors and potential effects on geodetic mass-balance measurements,” *J. Glaciol.*, vol. 67, pp. 613–626, 2021.

[15] J. Bannwart et al., “Elevation bias due to penetration of spaceborne radar signal on Grosser Aletschgletscher, Switzerland,” *J. Glaciol.*, vol. 70, Published online, pp. 1–40, 2024.

[16] S. Solberg, J. May, W. Bogren, J. Breidenbach, T. Torp, and B. Gizachew, “Interferometric SAR DEMs for forest change in Uganda 2000-2012,” *Remote Sens.*, vol. 10, no. 2, 2018, Art. no. 228.

[17] K. Karila, X. Yu, M. Vastaranta, M. Karjalainen, E. Puttonen, and J. Hyyppä, “TanDEM-X digital surface models in Boreal forest above-ground biomass change detection,” *ISPRS J. Photogrammetry Remote Sens.*, vol. 148, pp. 174–183, 2019.

[18] Y. Du et al., “Recent landslide movement in Tsaoling, Taiwan tracked by TerraSAR-X/TanDEM-X DEM time series,” *Remote Sens.*, vol. 9, no. 4, 2017, Art. no. 353.

[19] P. Potin, B. Rosich, N. Miranda, and P. Grimont, “Sentinel-1 mission status,” *Procedia Comput. Sci.*, vol. 100, pp. 1297–1304, 2016.

[20] P. Rizzoli, B. Bräeutigam, T. Kraus, M. Martone, and G. Krieger, “Relative height error analysis of TanDEM-X elevation data,” *ISPRS J. Photogrammetry Remote Sens.*, vol. 73, pp. 30–38, 2012. [Online]. Available: https://www.sciencedirect.com/science/article/pii/S0924271612001074

[21] C. Gonzalez and B. Bräutigam, “Relative height accuracy estimation method for InSAR-based DEMs,” *IEEE J. Sel. Topics Appl. Earth Observ. Remote Sens.*, vol. 8, no. 11, pp. 5352–5360, Nov. 2015.

[22] “Corine land cover 2018 vector, Europe,” 6-yearly. European Union’s Copernicus Land Monitoring Service information. [Online]. Available: https://doi.org/10.2909/71c95a07-e296-44fc-b22b-415f42acfdf0

[23] M. Martone, P. Rizzoli, and G. Krieger, “Volume decorrelation effects in TanDEM-X interferometric SAR data,” *IEEE Geosci. Remote Sens. Lett.*, vol. 13, no. 12, pp. 1812–1816, Dec. 2016.

[24] P. Rizzoli, M. Martone, H. Rott, and A. Moreira, “Characterization of snow facies on the Greenland ice sheet observed by TanDEM-X interferometric SAR data,” *Remote Sens.*, vol. 9, no. 4, Mar. 2017, Art. no. 315.

[25] G. Fischer, K. Papathanassiou, and I. Hajnsek, “Modeling multifrequency Pol-InSAR data from the percolation zone of the Greenland ice Sheet,” *IEEE Trans. Geosci. Remote Sens.*, vol. 57, no. 4, pp. 1963–1976, Apr. 2019.

[26] A. Ferretti, C. Prati, and F. Rocca, “Permanent scatterers in SAR interferometry,” *IEEE Trans. Geosci. Remote Sens.*, vol. 39, no. 1, pp. 8–20, Jan. 2001.

[27] M. Crosetto, O. Monserrat, M. Cuevas-González, N. Devanthéry, and B. Crippa, “Persistent scatterer interferometry: A review,” *ISPRS J. Photogrammetry Remote Sens.*, vol. 115, pp. 78–89, 2016. [Online]. Available: https://www.sciencedirect.com/science/article/pii/S0924271615002415

[28] J. Bueso-Bello, D. Carcereri, M. Martone, C. Gonzalez, P. Posovszky, and P. Rizzoli, “Deep learning for mapping tropical forests with TanDEM-X interferometric data,” *Remote Sens.*, vol. 14, no. 16, Aug. 2022, Art. no. 3981.

[29] G. B. M. Pedersen et al., “Volume, effusion rates and lava hazards of the 2021, 2022 and 2023 Reykjanes fires: Lessons learned from near real-time photogrammetric monitoring,” in *Proc. EGU Gen. Assem. EGU24*, 2024, p. 10724.

[30] “A computer-implemented method for calibrating a pair of digital elevation maps,” German Patent, DE 10 2023 123 310, Dec. 19, 2024.

Carolina González (Member, IEEE) received the Ingeniero Civil degree in telecommunication engineering from the Universidad Tecnica Federico Santa Maria, Valparaiso, Chile, in 2004.

In 2005, she joined Microwaves and Radar Institute, German Aerospace Center, Oberpfaffenhofen, Germany, in the System Engineering and Calibration (SEC) segment of TerraSAR-X taking care of the performance optimization. For the TanDEM-X mission, she worked first with Instrument Operations and Calibration Segment (IOCS) and later on in the Radar Science Group. She covered several aspects of the mission from system engineering, DEM performance and validation of global products to the edition of the global 30 m DEM and global Change Map products. Her research interests include large-scale products derived from SAR interferometry, DEM generation and calibration, artificial intelligence, snow parameters retrieval, and vegetation parameters estimation.

Luca Dell’Amore received the M.Sc. degree in information and communication engineering from the Universita degli Studi di Trento, Trento, Italy, in 2019. His master thesis entitled “Assessment of Image Quality of Waveform-Encoded Synthetic Aperture Radar (SAR) Using Real Data” has been pursued from Microwaves and Radar Institute, German Aerospace Center (DLR), Wessling, Germany.

Since 2021, he has been a Research Engineer with the Satellite SAR Systems Department, Microwaves and Radar Institute, DLR. He is currently working on performance investigation for the TerraSAR-X and TanDEM-X missions. His research interests include the development of innovative methods for Sentinel-1 data-based applications.

Mr. Dell’Amore was the recipient of the Young Scientist Awards at the International Radar Symposium and Kleinheubacher Tagung, both in 2019.

José-Luis Bueso-Bello received the Ingeniero degree in telecommunications engineering from the Universidad Politecnica de Valencia, Valencia, Spain, in 2003, and the M.Sc. degree in Earth oriented space science and technology from Technische Universität München, Munich, Germany, in 2007.

In 2003, he was with Microwaves and Radar Institute, German Aerospace Center, Oberpfaffenhofen, Germany, as System Engineer with the Department of Reconnaissance and Security, where he worked in the definition, design, and analysis for different SAR missions. In 2010, he was with Satellite SAR Systems Department, where he is currently a Project Engineer with main focus on the plan, evaluation, and performance monitoring of the TanDEM-X InSAR acquisitions. His research interests include signal processing, Earth system monitoring, and deep-learning algorithms with focus on the derivation of large-scale land-cover products from InSAR images.

Pietro Milillo (Senior Member, IEEE) received the bachelor’s (Laurea) and master’s degrees in physics, with a thesis on synthetic aperture radar and GPS data processing, from the University of Bari, Bari, Italy, in 2010 and 2012, respectively, and the Ph.D. degree in environmental engineering, with a thesis on the synergistic use of synthetic aperture radar constellations for studying natural and anthropogenic phenomena, from the University of Basilicata, Potenza, Italy, in 2016.

Over the years, he has held various positions, including NASA Postdoctoral Program Fellow with the

Jet Propulsion Laboratory (JPL), California Institute of Technology, Pasadena, CA, USA; a Scientist in radar science and engineering with JPL; and an Associate Project Scientist in Earth system science with the University of California, Irvine, CA, USA. Since 2021, he has been an Assistant Professor in civil and environmental engineering with the Department of Civil and Environmental Engineering, University of Houston (UH), Houston, TX, USA. He is also a Guest Scientist with the German Aerospace Center (DLR), Munich, Germany, and an Adjunct Professor in Earth and atmospheric science with UH. He has authored or coauthored more than 50 research articles in leading international journals. His research interests include synergistic use of remote sensing data exploitation and innovative approaches for computational analyses in Earth and cryosphere science and natural/anthropogenic hazard response. He is particularly interested in analyzing how the new generation of remote sensing instruments leads to a more effective, near real-time disaster monitoring, assessment, and response. His research interests, funded by NASA, DLR, and the Italian Space Agency, include Earth science, cryosphere, and disaster response.

Gabriele Schwaizer received a master's degree in meteorology and geophysics and the Ph.D. degree in natural sciences from the Leopold—Franzens University, Innsbruck, Austria, in 2007 and 2011, respectively.

From 2005 to 2009, she was University Tutor for theoretical meteorology and remote sensing in glaciology with the Institute for Meteorology and Geophysics, University of Innsbruck, Innsbruck, Austria. Since 2007, she has been a Scientist, and since 2011, a Senior Scientist with ENVEO-Environmental Earth Observation Information Technology GmbH, Innsbruck, Austria. She participated in several scientific field campaigns in the Alps and in Norway on glacier mass balance measurements and in preparation for new satellite systems. Her research interests, funded by ESA, the European Commission, and the Austrian Research Promotion Agency, include retrieval methods and applications of optical and microwave remote sensing for snow hydrology, climatology, monitoring glaciers from local to global scale, and assimilation of remote sensing products into geophysical process models.

Thomas Nagler (Member, IEEE) received the M.Sc. degree in meteorology and the Ph.D. degree in natural sciences from the University of Innsbruck, Innsbruck, Austria, in 1991 and 1996, respectively.

From 1991 to 2004, he was a Research Scientist with the Institute of Meteorology and Geophysics, University of Innsbruck. He is a Co-founder and, since 2001, Managing Director of ENVEO-Environmental Earth Observation Information Technology GmbH, Innsbruck, Austria. He has been a Principle/Co-investigator and Coordinator for several projects of ESA, the European Commission, and the Austrian Research Promotion Agency and for projects within ERS, ENVISAT ASAR, TerraSAR-X/Tandem-X, RADARSAT, ALOS PALSAR, and Copernicus Sentinel satellites. He is a Principal Investigator and Science Lead of the ESA CCI Snow project, and service Manager of the Copernicus Climate Change Service for the Cryosphere Domain. His research interests include retrieval methods and applications of active and passive microwave and optical remote sensing for snow hydrology, climatology, monitoring Alpine and polar glaciers and ice sheets, and assimilation of remote sensing products into geophysical process models.

Dr. Nagler is a Member of the ESA Mission Advisory Group for Sentinel-1 NG, ROSE-L, and ESA Earth Explorer 12 Candidate Mission Hydroterra+. He was Member of the EC Polar Expert Group I/II/III. He has participated in several scientific expeditions to Patagonia, Antarctica, and Alpine Glaciers, and was leading/participating in several international field campaigns in preparation for new satellite systems.

Paola Rizzoli (Member, IEEE) received the B.Sc. and M.Sc. degrees in telecommunication engineering from the Politecnico di Milano University (Polimi), Milan, Italy, in 2003 and 2006, repectively, and the Ph.D. degree (*summa cum laude*) in electrical engineering and information technology from the Karlsruhe Institute of Technology, Karlsruhe, Germany, in 2018.

From 2006 to 2008, she was the Scientific Researcher and Project Engineer with the Politecnico di Milano and Aresys s.r.l., a Polimi spin-off company. At the end of 2008, she joined the Microwaves and Radar Institute, German Aerospace Center (DLR), Oberpfaffenhofen, Germany, as Project Engineer, where she has been involved in the development and optimization of the TerraSAR-X and TanDEM-X missions, concentrating, in particular, on the generation of the TanDEM-X global digital elevation model. Since 2016, she has been leading the Radar Science Group of the Satellite SAR Systems Department, being responsible for the final performance assessment of the global TanDEM-X DEM and the generation of the global TanDEM-X Forest/Non-Forest map. Her research interests include SAR systems design, data reduction techniques, estimation theory, signal processing, and artificial intelligence algorithms.

Dr. Rizzoli was a recipient of the DLR Science Award in 2018, the Best Paper Award at the German Microwave Conference in 2019, and the Best Poster Award at the ESA Worldcover Conference in 2017. She regularly serves as a Reviewer for the IEEE TRANSACTIONS ON GEOSCIENCE AND REMOTE SENSING, the IEEE GEOSCIENCE AND REMOTE SENSING LETTERS, and the IEEE JOURNAL OF SELECTED TOPICS IN APPLIED EARTH OBSERVATIONS AND REMOTE SENSING.